# Left Handed Metamaterials in Microstrip Patch Antenna Design: Miniaturization, Multiband Operation, and Improved Performance

**Nusrat Jahan Shimu[1], Pankaj Chandra Kar[2], Md. Ariful Islam[3*] and Anis Ahmed[4]**

[1]Department of Oceanography, University of Dhaka, Dhaka-1000, Bangladesh
[2]Department of Information and Communication Technology, Comilla University, Cumilla, Bangladesh
[3]Department of Robotics and Mechatronics Engineering, University of Dhaka, Dhaka-1000, Bangladesh
[4]Department of Electrical and Electronic Engineering, University of Dhaka, Dhaka-1000, Bangladesh

[*]Email: arif.rme@du.ac.bd

Received on 14 May 2023, Accepted for Publication on 25 January 2024

## ABSTRACT

**The exotic electromagnetic properties of metamaterials (MTM) can be utilized to meet the increasing demand for smaller, lighter, and more compact multiband antennas. As the resonant frequency is dependent on the aperture parameters of the antenna, metamaterials allow for the miniaturization and performance enhancement of antennas. In this paper, two novel designs of metamaterial loaded microstrip patch antennas are proposed. The first structure emphasizes the miniaturization of patch antennas with performance improvements. The second one deals with the multiband operation of metamaterial loaded antennas with wider bandwidth and improved performance. Compared to the conventional microstrip patch antenna (MPA), the proposed metamaterial loaded antenna has reduced the size by 75%, and antenna characteristics have also improved significantly. The proposed metamaterial antenna resonates at 2.45 GHz, the return loss is -26 dB, and a gain of 5.28 dB is achieved. The multiband antenna can be realized by etching different numbers of complementary split ring resonators in the ground plane. The model proposed with three split ring resonators (SRR) at the ground plane shows quad band operations and can be used in S-band and C-band simultaneously. The quad-band antenna resonates at 3.04 GHz, 3.42 GHz, 5.35 GHz, and 6.08 GHz with bandwidths of 78 MHz, 93 MHz, 167 MHz, and 185 MHz, respectively. The antennas are designed on an FR-4 substrate with a permittivity of 4.3. Nicolson-Ross-Weir (NRW) method has been employed for the extraction and verification of the metamaterial properties of the unit cells. Due to its ability to capture more energy, the reported antenna can be used as a wireless device as well as an RF energy harvesting device.**

**Keywords:** Metamaterials, Multiband antennas, Microstrip antenna, FR-4 substrate, Resonator

## 1. Introduction

In the context of the rapidly evolving wireless communication landscape, the demand for compact, versatile antennas capable of accommodating multiple standards and operations has grown significantly. This necessity is underscored by the emergence of cognitive radio (CR) services, which call for intelligent spectrum detection and allocation [1]. To address the challenges associated with wider bandwidths, conventional approaches require separate RF filters to mitigate out-of-band signals, often limiting adaptability. A novel solution is presented here, whereby an antenna's orientation can be easily adjusted to achieve optimal performance, obviating the need for front-end RF filters [2]. Capitalizing on the unique properties of metamaterials, it becomes possible to engineer resonant frequencies that enable antennas to function across diverse frequency ranges simultaneously [3]. These materials exhibit exceptional electromagnetic characteristics, furnishing the groundwork for the development of smaller, more efficient, and performance-enhancing antennas, leveraging attributes such as negative permeability and permittivity for applications like dielectric property sensing [4].

Illustrative prior research includes the work by Huda A. Majid et al. (2008) [5], who devised and simulated a left-handed metamaterial (LHM) augmented single-MPA configuration. Through the integration of modified square rectangular split rings (RSR) and capacitance-loaded strips (CLS), these researchers achieved negative permeability and permittivity values, resulting in a gain augmentation of 4 dB when LHM was incorporated. The addition of LHMs was found to focus radiation, reducing the half-power beam width (HPBW) from 80 to 40 degrees, although accompanied by introduced side and rear lobes that could potentially be minimized to further enhance gain. Moreover, Roman Kubacki et al. (2017) [7] presented a pioneering approach yielding an antenna with a remarkable bandwidth spanning from 4.1 GHz to 19.4 GHz, accompanied by a gain reaching 6 dBi and a peak of 10.9 dBi. This innovation notably surpassed the performance and bandwidth capabilities of conventional MPAs by a factor of 68, demonstrating improved radiation efficiency over a broad horizontal span of 270 degrees. Further advancing the field, A. H. Rambe et al. (2023) [9] formulated a circularly polarized single MPA enhanced through the integration of a patch-section complementary split ring resonator (CSRR). This specialized component exhibited suitability for GPS applications, characterized by a slender 1.6 mm thickness, FR-4 substrate composition, and resonant frequency of 1.57 GHz. Remarkably, the complementary SRR metamaterial architecture yielded a substantial reduction in return loss, achieving levels as low as -40.92 dB within the 1.56–1.59 GHz range, consequently effecting a 36% reduction in substrate size and a 46% reduction in patch dimensions. In light of these innovative antecedents, the present work aims to contribute to the evolving landscape of antenna design through the exploration of metamaterial-embedded

configurations, with a focus on size reduction, multifunctionality, and enhanced performance.

**Table 1:** A comparison of the work to be proposed with the work that has already been published

| Authors | Multi-band operation | Miniaturization | Improving radiation characteristics | Bandwidth Improvement |
|---|---|---|---|---|
| E. Dogan et al., (2013) [7] | No | Yes | Yes | Yes |
| Roman Kubacki et al., (2017) [8] | No | No | Yes | Yes |
| A H Rambe et al., (2023) [9] | No | Yes | Yes | Yes |
| Trushit Upadhyaya et al., (2022) [10] | No | Yes | Yes | Yes |
| Proposed Work | Yes | Yes | Yes | Yes |

In response to the growing demand for compact multiband antennas, this paper presents two innovative designs of metamaterial-loaded microstrip patch antennas aiming for size reduction and enhanced performance. By integrating resonant metamaterial structures, these antennas modify the standard resonant state, achieving a size reduction of 75% with improved gain (proposed antenna 1) and enabling multiband operation, enhanced bandwidth, isolation, compactness, and reduced mutual coupling through the use of multiple SRR structures (proposed antenna 2). Comparative analysis demonstrates the superiority of metamaterial-loaded patch antennas over conventional ones, exhibiting smaller size, more operating bands, and higher gain. Moreover, the incorporation of parallel double split ring resonators facilitates RF energy harvesting, rendering the antenna suitable for high signal attenuation scenarios and potential rectenna applications.

## 2. Metamaterials

The characteristics of a MPA are its length, width, input impedance, gain, and radiation patterns. The effective dielectric constant $\varepsilon_{reff}$, characteristic impedance $Z_0$, width of the patch $W$, and effective length $L_{eff}$ for the conventional microstrip patch antenna presented in this paper are calculated using the equations from [11].

Metamaterials are synthetic, efficient, homogeneous structures with unusual electromagnetic properties, in contrast to natural materials, whose intrinsic characteristics depend on their chemical composition. They attain their homogeneity from the unit cell, whose size is much smaller than the wavelength of the incident electromagnetic wave [12]. Double negative (DNG)/left-handed materials ($\varepsilon < 0$, $\mu < 0$) are known as metamaterials that lie in quadrant III (Fig. 1).

For plane waves, the simultaneous positive values of $\varepsilon$ and $\mu$ and the electric field $E$, magnetic field $H$ and propagation vector $k$ make a right handed orthogonal system (quadrant I).

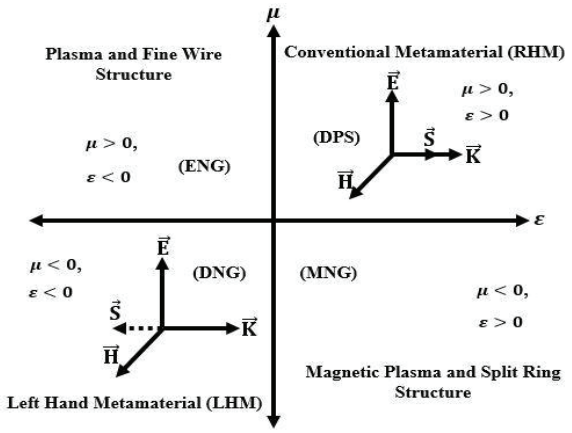


**Fig. 1.** Permittivity-permeability (ε-μ) and refraction index (n) diagram.

As the metamaterial shows simultaneous negative values of $\varepsilon$ and $\mu$, Maxwell's equation reduces to [13]

$$k \times E = -\omega|\mu|H \qquad (1)$$
$$k \times H = \omega|\varepsilon|E$$

This indicates that the $E$, $H$, and $k$ form a left-handed triplet. For simultaneous changes of sign of permittivity and permeability, the direction of energy flow $S$ is not affected; therefore, the group velocity will be positive for both left-handed and right-handed systems. Refractive index is given as [13]

$$n = \pm\sqrt{\varepsilon\mu} \qquad (2)$$

And phase velocity is given as [13]

$$v_p = \frac{c}{n} \qquad (3)$$

Where $c$ is the velocity of light in vacuum. For left-handed systems, $n$ is negative, so the phase velocity is negative. Hence the direction of energy flow and the wave will be opposite, resulting in backward wave propagation, i.e., the vectors of the electric and magnetic fields and the wave vector form a left-oriented set, contrary to conventional materials (right-handed) [13].

### *2.1 Metamaterial Unit Cell Structure*

Combining electric and magnetic dipole elements allows for the synthesis of metamaterial substrates. Magnetic dipoles are split-ring resonators (SRRs) and slot lines, while electric dipoles are metal wire lines and complementary split-ring resonators (CSRRs) [14].

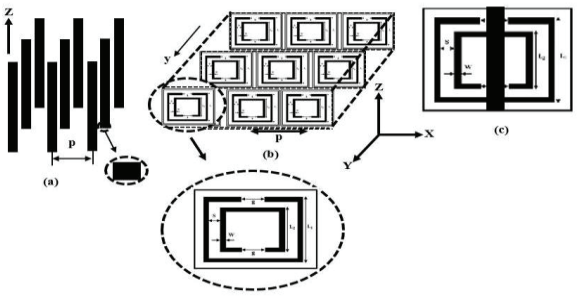


**Fig. 2.** Metamaterials with (a) negative permittivity and positive permeability, (b) negative permeability and positive permittivity; and (c) double negative media (DNG) [15].

In the structure shown in Fig. 2(a), if the excitation of the electric field ***E*** is parallel to the axis of the wires (**E**||z) we have [15]:

$$\varepsilon_r(\omega) = 1 - \frac{\omega_{pe}^2}{\omega^2 + j\omega\zeta} = 1 - \frac{\omega_{pe}^2}{\omega^2+\zeta^2} + j\frac{\zeta\omega_{pe}^2}{\omega(\omega^2+\zeta^2)} \quad (4)$$

Where, $\omega_{pe} = \sqrt{\frac{2\pi c^2}{[p^2 ln ln\left(\frac{p}{r}\right)]}}$ is the electric plasma frequency, $\zeta = \frac{\varepsilon_0\left(\frac{p\omega pe}{r}\right)^2}{\pi\sigma}$ is the damping factor due to metal losses, $c$ = speed of light, and $r$ = radius of the wire. The positive-$\varepsilon$/negative-$\mu$ MTM is the metal split-ring resonator (SRR) structure shown in Fig. 2(b). If the excitation of the magnetic field ***H*** is perpendicular to the plane of the rings (**H**⊥ $y$) [16].

$$\mu_r(\omega) = 1 - \frac{F\omega^2}{\omega^2 - \omega_{0m}^2 + j\omega\zeta} = 1 - \frac{F\omega^2(\omega^2-\omega_{0m}^2)}{(\omega^2-\omega_{0m}^2)^2+(\omega\zeta)^2} + j\frac{F\omega^2\zeta}{(\omega^2-\omega_{0m}^2)^2+(\omega\zeta)^2} \quad (5)$$

Where, F = $\pi$(r/p)$^2$, (r: inner radius of the smaller ring), $\omega_{0m} = c\sqrt{\frac{3p}{\pi ln\,(2dr^3/s)}}$ is the magnetic resonance frequency.

### *2.2 Nicolson-Ross-Weir (NRW) Method*

The correlation between S-parameters and material properties is derived by considering multiple reflections of a unit amplitude wave incident upon the sample interfaces within a waveguide [17]. From the S parameters $S_{11}$ and $S_{21}$, first we calculate two composite terms $V_1$ and $V_2$.

$$V_1 = S_{21} + S_{11}$$
$$V_2 = S_{21} - S_{11} \quad (6)$$

The electrical thickness of the MTM slab is not too large and the complex wavenumber $k$, transmission term $Z$, are used to obtain the approximate results for the wave impedance $k$ and permeability $\mu_r$ from the following equations respectively [18]

$$k \sim \frac{1}{jd}\frac{(1-V_1)(1+\Gamma)}{1-\Gamma V_1} \quad (7)$$
$$\mu_r \sim \frac{2}{jk_0 d}\frac{1-V_2}{1+V_2}$$

In the above equations, interface reflection coefficient $\Gamma = \frac{Z-V_2}{1-ZV_2}$. Then the permittivity $\varepsilon_r$ and index of refraction $n$ can be obtained as [19]

$$\varepsilon_r = \left(\frac{k}{k_0}\right)^2 \frac{1}{\mu_r} \quad (8)$$
$$n = \sqrt{\varepsilon_r\mu_r} = \frac{k}{k_0}$$

## 3. Simulation and Results Analysis

This section details the design methodology employed for this research, including a description of the selected MTM unit cell structures, simulations of conventional and proposed MTM antennas, and an analysis of the simulation results. Computer simulation technology, microwave studio (CST MWS), is utilized to conduct the simulation. The design has been optimized accordingly to meet the theoretical expectation.

The CST software simulation includes the following features:

I. Design of a Circular and a Square SRR unit cell.
II. 2.45 GHz conventional MPA design
III. Design of the proposed MTM loaded MPA at 2.45 G Hz.
IV. Design of proposed MTM-loaded multiband antenna with a larger bandwidth.

The design of MTM antennas is carried out by determining the metamaterial response of a substrate with negative permittivity $\varepsilon_r$, and permeability $\mu_r$ [3]. First, two SRR unit cells (one circular and one square) are designed in the simulation process. The extracted parameters then demonstrate that the SRR unit cells exhibit metamaterial properties [3]. These two SRRs will then be incorporated into the ground plane of a rectangular MPA for miniaturization and performance enhancement.

### 3.1 Design and Simulation of MTM Unit Cell

The target parameter is for the substrate to exhibit metamaterial behavior between 2.45 and 3.2 GHz. In Table 2, the characteristics and parameters of the substrate are detailed. The resonant frequency of SRR is dependent on the ring radius, ring width, and slit width. Increasing the ring's radius decreases its resonant frequency. Again, the resonance frequency increases with the ring's width.

**Table 2:** Characteristic parameters of the FR-4 substrate

| **Characteristics** | **Values** |
|---|---|
| Permittivity($\varepsilon_r$) | 4.3 |
| Permeability( $\mu_r$) | 1 |
| Loss tangent, ($\delta$) | 0.002 |
| Substrate height($h$) | 1.6 mm |
| Copper cladding($t$) | 0.035 mm |

Variations in slit width have less of an effect on the resonant frequency. Both the circular and square SRR resonates at 2.45 GHz. The dimensions of the two structures are provided in Table 3.

**Table 3:** Dimensions of the designed SRR unit cell parameters

| **Circular SRR unit cell** | | **Square SRR unit cell** | |
|---|---|---|---|
| **Parameter** | **Value (mm)** | **Parameter** | **Value (mm)** |
| Radius of the the outer ring ($r_1$) | 5.2 | Length of outer ring ($l_1$) | 5.5 |
| Radius of the inner ring ($r_2$) | 3.2 | Length of inner ring ($l_2$) | 4.1 |
| Ring width ($c$) | 1 | Ring width ($w$) | 0.6 |
| Split width ($d$) | 1 | Split width ($s$) | 0.1 |
| Gap ($g$) | 0.5 | Gap ($g$) | 0.5 |
| Wire width | 1 | Wire width ($W_w$) | 1 |
| Wire length | 12 | Wire length ($L_w$) | 6 |

### *3.2 Equivalent Circuit of MTM Unit Cell*

Figs. 3(a) and 3(b) and Figs. 4(a) and 4(b) depict circular SRR and square SRR schematic geometry and an analogous circuit, respectively. The electrically tiny structure of the SRR resonates due to loop inductance and effective capacitance across the loop gap [21]. These LC circuits simulate the behavior of a resonant cavity. A magnetic field H perpendicular to the plane between the two split rings creates a gap capacitor $C_g$ or $C_{gap}$ at each ring's gap. A mutual capacitor $C_P$ connects these metal rings. Each ring resembles a solenoid with inductance $L_m$ and surface capacitance $C_m$ for both circular and square rings. In dielectric materials, the inductance remains unchanged, but the capacitance changes with permittivity. Based on circuit properties, the elements of the proposed model can be determined. Line inductance is $L$, while coupling capacitance between microstrip line and circular SRR is $C_C$.

By analyzing the split ring resonator, as done in [16]-[19], the structure of the equivalent circuit elements can be determined.

For circular SRR,

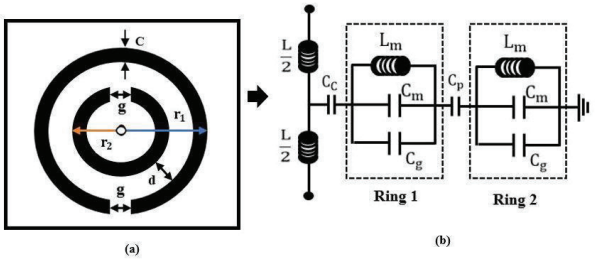


**Fig. 3.** (a) Schematic geometry of the circular SRR, (b) Equivalent circuit of the circular SRR

For Square SRR,

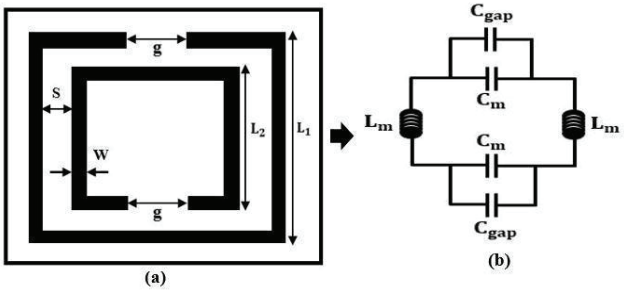


**Fig. 4.** (a) Schematic geometry of square SRR; (b) Equivalent circuit of square SRR

**Table 4:** The expression for equivalent circuit of circular and square SRR

| Parameters | Circular SRR | Square SRR |
|---|---|---|
| Inductance of the closed ring, $L_m$ | $\mu_0(R - \frac{C}{2}) \times \{ln[\frac{R-\frac{C}{2}}{d+c}] - 0.5\}$ | $\frac{\mu_0 S}{W}(l_1+l_2)$ |
| Gap Capacitance, $C_g$ | $\approx \frac{\varepsilon_0 ct}{g}$ | $\approx \frac{\varepsilon_0 wt}{g}$ |
| Surface Capacitance, $C_{surf}$ or $C_m$ | $\approx \frac{2\varepsilon_0 d}{\pi} ln\,[\frac{R-C}{g}]$ | $\frac{A\varepsilon_0 W(2l_1+2l_2}{2S}$ |
| Resonant Frequency, $f_r$ | $\frac{1}{2\pi\sqrt{L_m(C_m+C_g)}} \approx \frac{1}{2\pi\sqrt{L_m C_m}}$ | $\frac{1}{2\pi\sqrt{L_m(C_m+C_g}} \approx \frac{1}{2\pi\sqrt{L_m C_m}}$ |
| Equilibrium Constant, $A$ | - | $\frac{C^2}{4\pi^2(l_1+l_2)f_0^2\varepsilon_r}$ |

**Table 5:** Dimensions of the elements of the equivalent circuit of the proposed SRR in Figs. 3(b) and 4(b)

| Parameters | $L_m$ | $C_m$ | $C_g$ | $f_r$ |
|---|---|---|---|---|
| **Circular SRR** | 1.5 nH | 2.8 pF | 0.6 fF | 2.45 GHz |
| **Square SRR** | 2 nH | 2.2 pF | 0.4 fF | 2.45 GHz |

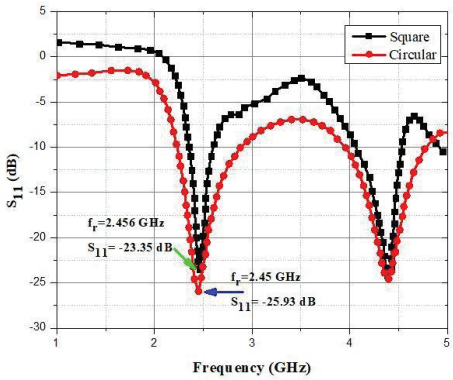


**Fig. 5.** Frequency response of the circular and square SRR

### *3.3 Simulation and Parameter Extraction of Circular SRR*

The simulated S-parameter values from CST are exported to the Matlab environment. Then, the NRW method is used to derive the SRR unit cell's permittivity, permeability, index of refraction, etc. SRRs are designed to have resonant responses at specific frequencies, i.e. at 2.45 GHz. When an electromagnetic wave interacts with the SRR structure, at these resonant frequencies, a strong coupling between the incident wave and the resonant elements of the SRRs. The split in the ring creates capacitance, while the metallic segments act as inductors. This arrangement leads to a localized magnetic field inside the split ring and an electric field across the split.

From Fig. 6(a), it can be seen that the SRR unit cell operates as a double negative medium between 2.45 GHz and 2.73 GHz, and as a single negative metamaterial between 2.73 GHz and 3.27 GHz. At the resonant frequencies, the interaction between the SRR structure and the incident wave results in an effective medium behavior that can exhibit negative permittivity ($\varepsilon$), negative permeability ($\mu$), and a negative refractive index ($n$). The negative values arise due to the out-of-phase response, which causes the SRR structure to behave as a metamaterial with unique electromagnetic properties. If both the unit cell permittivity and permeability are negative, then the unit cell has a negative index of refraction. Fig. 6(b) depicts the simulated SRR refraction index vs. frequency curve.

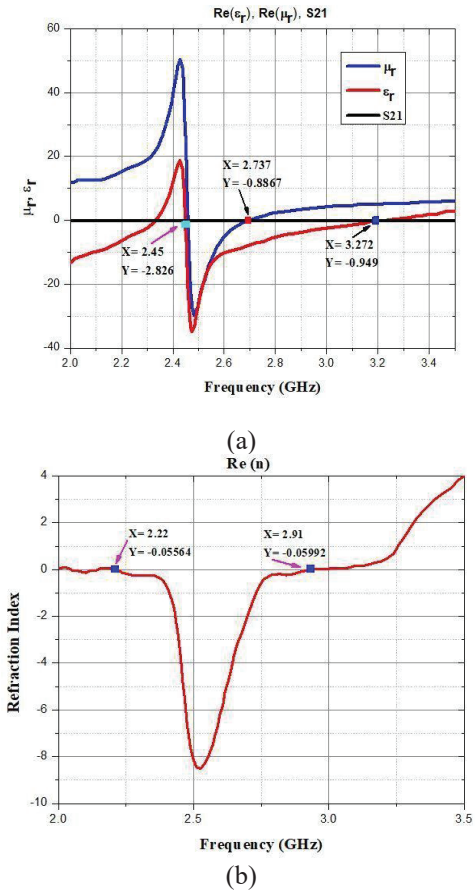


**Fig. 6.** Parameter extraction of circular SRR (a) relative permittivity, permeability vs. frequency, and (b) refraction index vs. frequency

### *3.4 Simulation and Parameter Extraction of Square SRR*

The split in the square ring (Fig. 4(a)) creates an effective LC circuit, with inductance and capacitance elements. At the resonant frequency, the SRR structure exhibits an effective magnetic response due to the circulating currents induced in the ring. This response is responsible for the negative permeability. Both the effective permeability and permittivity are negative near the peak value; thus, the refractive index has a negative value ($n$<0), exhibiting the LH behavior. The red line in Fig. 7(a) represents the relative permittivity ($\varepsilon_r$), while the blue line represents the permeability ($\mu_r$) value. According to the graph, the unit cell exhibits negative $\varepsilon_r$ values between 3.12 GHz and 4.78 GHz and negative $\mu_r$ between 3.16 GHz and 3.64 GHz. Consequently, the SRR unit cell behaves as an LH medium between 3.12 GHz and 4.78 GHz. The negative permittivity, permeability, and refractive index observed in square-shaped split ring resonators are a result of resonance phenomena and effective medium theory, which collectively produce unique electromagnetic responses in these metamaterial structures.

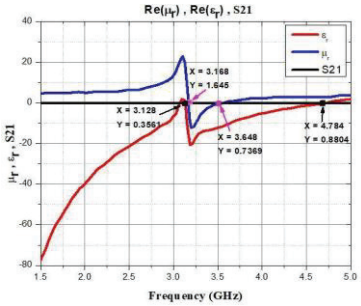


(a)

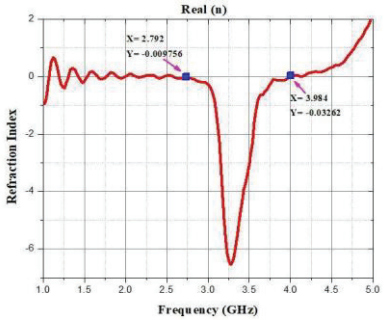


(b)

**Fig. 7.** Parameter extraction of square SRR (a) relative permittivity, permeability vs. frequency, (b) refraction index vs. frequency.

### *3.5 Design of Conventional MPA and Proposed MTM Antenna at 2.45 GHz*

The design of the conventional MPA at 2.45 GHz is intended for comparison with the MTM-loaded antenna. These structures consist of an FR-4 substrate with a dielectric constant of 4.3 and a thickness of 1.6 mm. Utilizing a microstrip line feed mechanism, a 50 Ω waveguide port supplies power to the radiator patch. Fig. 8 depicts the various design parameters for the proposed and conventional antennas, and Table 6 lists the corresponding antenna dimensions. To reduce the size of the patch antenna, the circular SRR unit cell designed and simulated in the previous section is etched in the ground's center. According to Table 6, the overall and patch dimensions of a conventional antenna are (78mm x 58 mm) and (40 mm x 28 mm). This conventional MPA has a 2.45 GHz resonance. The SRR structure can act as a capacitor, which can increase the effective capacitance of the antenna and help reduce its physical size. The SRR structure can modify the current distribution on the patch and ground plane, resulting in more efficient use of the available surface area and a reduction in the physical size of the antenna.

**Table 6:** Dimensions of conventional and MTM loaded antennas

| Parameter | Symbol | Conventional antenna | Proposed MTM antenna |
|---|---|---|---|
| Substrate width | $W_s$ | 78 mm | 39 mm |
| Substrate length | $L_s$ | 58 mm | 28 mm |
| Patch width | $W_p$ | 40 mm | 23 mm |
| Patch length | $L_p$ | 28 mm | 14 mm |
| Feed line width | $W_f$ | 3.2 mm | 1.7 mm |
| Inset length | $f_i$ | 9.2 mm | 4 mm |

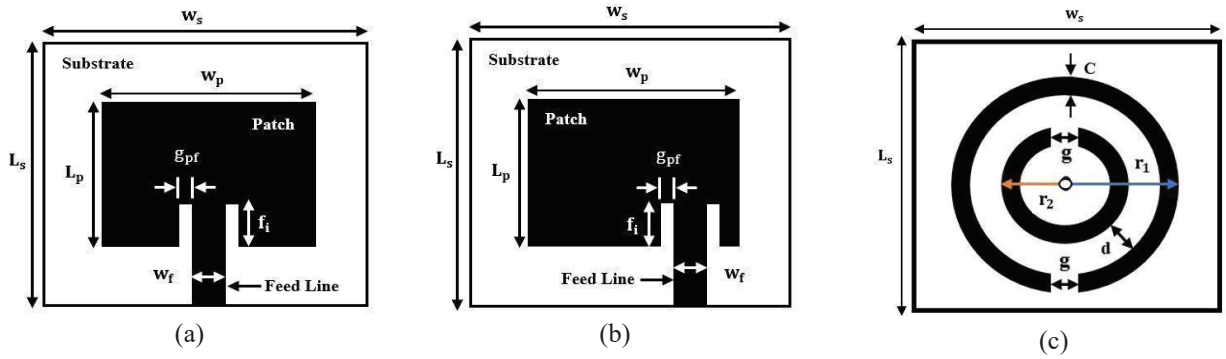


**Fig. 8.** (a) Conventional MPA; (b) Proposed MTM antenna (top view); (c) Proposed MTM antenna (bottom view).

### *3.6 Simulation Results and Comparison between Conventional MPA and Proposed MTM Loaded Antenna*

#### *3.6.1 Return Loss and Bandwidth*

When a SRR is integrated into the ground plane of a patch antenna, it can alter the current distribution and electromagnetic fields around the antenna, which can improve the antenna's impedance matching and reduce its return loss. Fig. 9 compares the return loss $S_{11}$ responses of conventional and proposed MTM antennas. Based on the graph, the normal antenna has a return loss of -18 dB at 2.45 GHz resonance. In contrast, the return loss of the MTM antenna at the same operating frequency of 2.45 GHz is -26 dB.

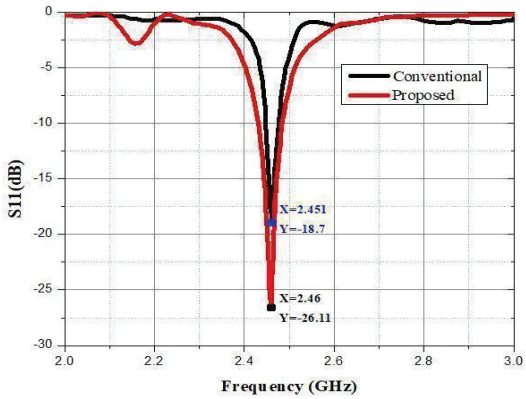


**Fig. 9.** Return loss ($S_{11}$) vs. frequency for conventional antenna and metamaterial antenna.

#### *3.6.2 Radiation Pattern*

The radiation pattern shows the direction of the maximum radiation intensity of the antenna. The SRR structure can help suppress surface wave radiation, which can reduce the loss of power from the antenna and improve its directivity.

The conventional antenna has a far-field directivity of 7.09 dBi, while the MTM antenna has a far-field directivity of 7.16 dBi and a side lobe level of -10.4 dB. The inherent property of metamaterials is to control the direction of electromagnetic radiation and collect the emitted energy in a smaller angular domain. In MTM antennas, the directivity has increased as a result. The SRR structure acts as a resonant structure that can increase the effective size of the ground plane of the patch antenna. This increased size can help reduce the effects of edge diffraction, which can improve the gain and directivity of the antenna. The resonant nature of the SRR structure can also enhance the coupling between the patch and the ground plane, leading to improved radiation efficiency.

Figs. 10(a) and 10(b) illustrate, respectively, the far-field gain properties of a conventional MPA antenna and the proposed MTM antenna. The far-field gain of a conventional antenna is 3.79 dB, the main lobe direction is 1.0 degrees, and the angular width is 93.5 degrees. For MTM antennas, the far-field gain is 5.28 dB, and the principal lobe direction is 1.0 degrees. And the angle width is 89.7 degrees. The MTM structure increases the amount of power coupled to the space wave while decreasing the surface wave effects. Consequently, antenna gain has increased from 3.79 dB to 5.28 dB as a result of utilizing MTM.

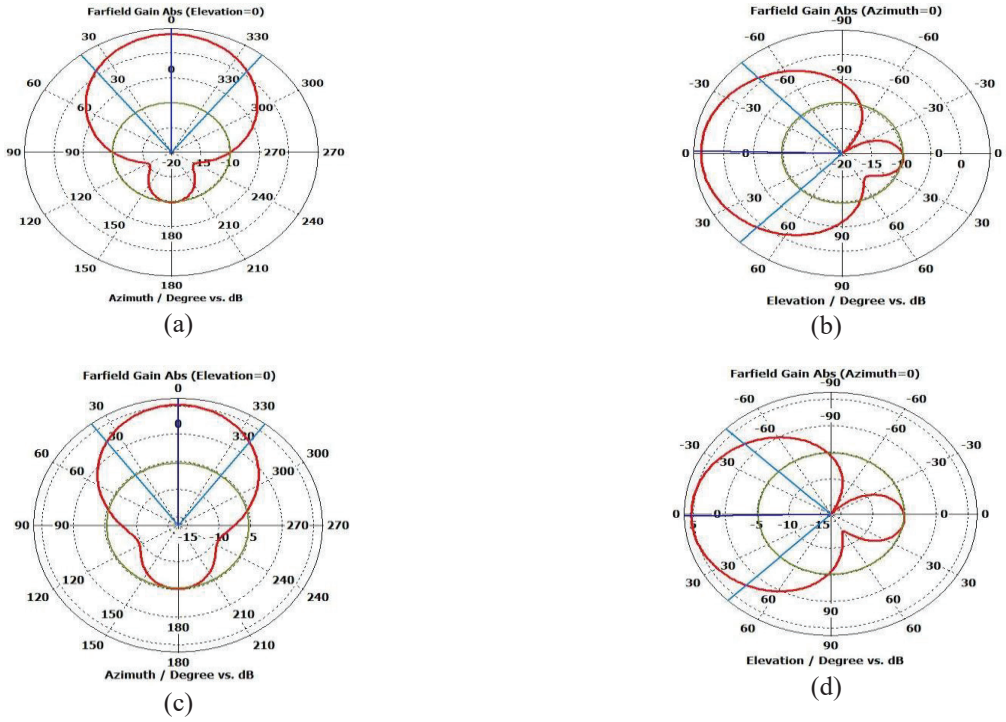


**Fig. 10.** Far-field radiation pattern (Gain), (a) Elevation plane, (b) Azimuth plane of Conventional antenna, (c) Elevation plane, (d) Azimuth plane of MTM antenna

**Table 7:** Comparison between the radiation patterns of conventional and proposed MTM antennas

| Parameter | | Conventional Antenna | MTM Antenna |
|---|---|---|---|
| **Azimuth angle/dB** | Main lobe | 3.79 dB | 5.27 dB |
| | Main lobe direction | 0.0 deg | 0.0 deg |
| | Angular width (3dB) | 76.2 dB | 73.8 dB |
| | Side lobe level | -13.7 dB | -10.5 dB |
| **Elevation angle/ dB** | Main lobe | 3.79 dB | 5.27 dB |
| | Main lobe direction | -1.0 deg | 1.0 deg. |
| | Angular width (3dB) | 93.5.2 dB | 89.7 dB |
| | Side lobe level | -13.5 dB | -10.4 dB |

Table 8 compares the overall performance characteristics of the standard patch antenna and the reported MTM antenna. Normal and MTM antennas resonate at the same frequency, but the size of the MTM antenna (.32$\lambda_0$ x .23$\lambda_0$) is nearly 75% smaller than the size of the patch antenna (.64 $\lambda_0$ x .48 $\lambda_0$), indicating that the use of MTM unit cells has resulted in a reduction in antenna size. The SRR structure can modify the current distribution on the patch and ground plane, resulting in a higher resonant frequency for the patch antenna. This allows for the use of smaller patch sizes while maintaining the desired operating frequency.

**Table 8:** Overall Comparison between the performance of conventional and proposed MTM antennas

| Parameter | Conventional antenna | MTM antenna |
|---|---|---|
| Size (mm × mm) | 78×58 | 39×28 |
| Resonant frequency (GHz) | 2.450 | 2.456 |
| Return loss (dB) | -18 | -26 |
| Bandwidth (MHz) | 64 | 57 |
| VSWR | 1.26 | 1.10 |
| Directivity (dBi) | 7.09 | 7.16 |
| Gain (dB) | 3.79 | 5.28 |
| Total efficiency | 45% | 60% |

The return loss ($S_{11}$) of the proposed MTM antenna is -26 dB compared to -18 dB for a conventional patch antenna. Normal antenna bandwidth is 64 MHz, while MTM antenna bandwidth is 57 MHz. The MTM antenna has a VSWR value of 1.1, which is also superior to the 1.26 value of a standard patch antenna. The SRR structure can reduce surface wave radiation and modify the current distribution on the patch, resulting in improved directivity and better radiation efficiency. The MTM antenna has also improved the total antenna efficiency to 60%.

Overall, putting an SRR structure in a patch antenna's ground plane can improve its performance in many ways, such as by making it smaller, increasing its bandwidth, improving its gain and directivity, reducing its mutual coupling, and reducing its back radiation.

To validate the microstrip patch antenna designed in CST, the conventional patch antenna is fabricated on FR-4 substrate and tested using Wave and Antenna Training System (WATS-2002). Due to some unavoidable limitations, we couldn't measure the proposed metamaterial antenna. The radiation pattern after measurement is presented in Fig. 11 (b). The measured radiation pattern resembles the simulated radiation pattern, with a directive front lobe and a smaller back lobe.

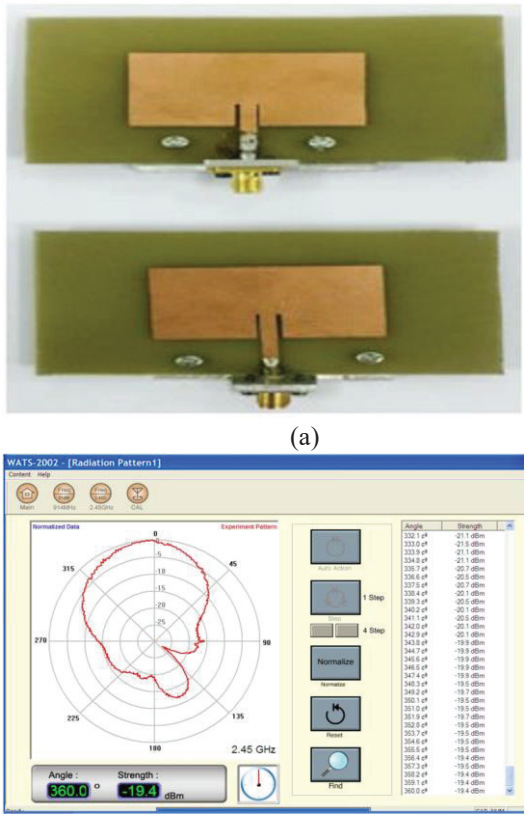


(a)

(b)

**Fig. 11.** Measurement results of the conventional antenna, (a) Top view of the fabricated antenna, (b) Radiation pattern of the measured antenna

### *3.7 Antenna Structure for Multiband Applications*

Currently, the technologies of wireless communication systems are expanding rapidly to support multimedia, image, speech, and data communication over wider bandwidths and at higher transmission rates. To meet the ever-increasing demand, an antenna must be able to operate in multiple frequency bands. The SRR structure in the ground plane can provide additional resonant frequencies that can be used to create multiple operating bands for the patch antenna. The resonant frequency of the SRR structure can be adjusted by changing its dimensions, allowing for flexibility in the design of the antenna.

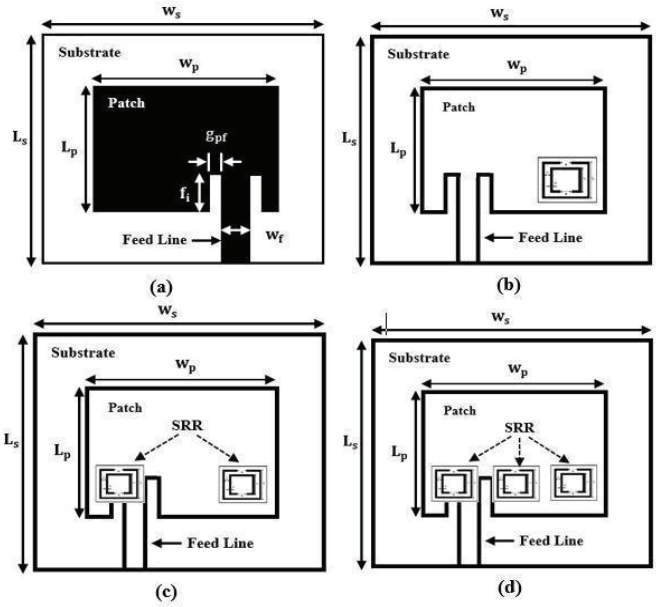


**Fig. 12.** Proposed multiband MTM MPA configuration, (a) Top view of all three configurations, (b) Model-1, bottom view with one Square SRR, (c) Model-2, bottom view with two Square SRR, (d) Model-3, bottom view with three Square SRR.

The square SRR simulated in the previous section (Fig. 4(a)) is incorporated into the configuration of the compact patch antenna. By altering the location and number of SRRs on the ground plane, various structures have been tested. The objective is to achieve the optimal outcome and evaluate the performance of various configurations. Fig. 12(a) depicts the top views of all three designed structures. Figs. 12 (b), 12 (c), and 12 (d) depict the bottom view and position for one, two, and three SRRs, respectively.

**Table 9:** Patch and SRR dimensions for multiband antennas

| **Patch dimension** | | **Square SRR dimension** | |
|---|---|---|---|
| Parameter | Value (mm) | Parameter | Value (mm) |
| Substrate width ($W_s$) | 39 | Outer ring length ($l_1$) | 5.5 |
| Substrate length ($L_s$) | 28 | Inner ring length ($l_2$) | 4 |
| Patch width ($W_p$) | 18.6 | Split width ($s$) | 0.1 |
| Patch length ($L_p$) | 14 | Ring width ($w$) | 0.6 |
| Feed line width ($W_f$) | 1.7 | Gap ($g$) | 0.5 |

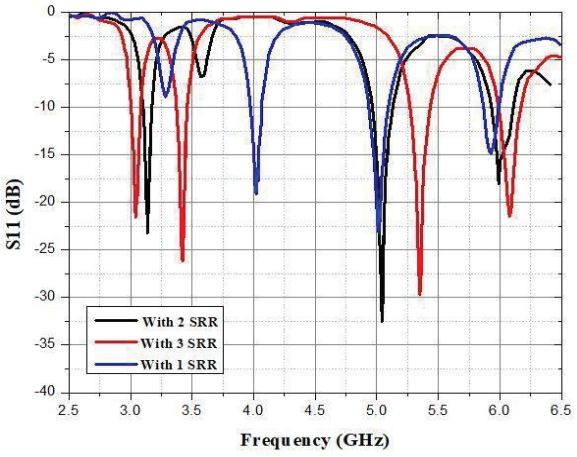


**Fig. 13.** Return loss (S11) vs. frequency for different configurations of MTM loaded multiband antennas

Fig. 13 depicts the relationship between $S_{11}$ (dB) and frequency (GHz) for various positions and numbers of SRR, and Fig. 14 shows the surface current distribution for the varying number of SRRs in the ground plane. The $S_{11}$ curve reveals that the number of resonant frequencies increases as the number of SRRs increases. By adding multiple SRR structures to the ground plane of a patch antenna, additional resonant frequencies can be generated that cover a wider frequency range. A strategic arrangement of multiple SRRs can regulate their coupling and permit the design of antennas that operate independently in separate frequency bands without interfering with each other. This can help improve isolation between operating bands, resulting in reduced interference and improved performance.

When multiple SRRs are utilized, localized regions of enhanced electromagnetic fields can be generated. This localization contributes to the overall surface current distribution by concentrating surface current trajectories around SRRs. It can be observed that most surface currents are concentrated on the edges of the interior and exterior of square SRR slots. Interactions between SRRs result in current paths that couple the SRRs, leading to a unique current distribution.

Model-1 (with 1 SRR) exhibits resonance at 4.03 GHz, 5.02 GHz, and 5.93 GHz, respectively (Table 10), and the corresponding BW is 95 MHz, 158 MHz, and 126 MHz. At the resonant frequencies, the total antenna efficiency is 50%, 51%, and 35%, respectively.

Model-2 resonates in the triple band, with narrow bandwidth at lower resonating frequencies and broad bandwidth at higher resonating frequencies. Model-2 with two SRRs at the ground has improved return losses of -23 dB, -32 dB, and -36 dB at 3.13 GHz, 5.04 GHz, and 6.03 GHz, respectively. Thus, the proposed model operates simultaneously in the S-band and the C-band.

For Model-3, resonant frequencies are 3.04 GHz, 3.42 GHz, 5.35 GHz, and 6.08 GHz. This model exhibits the highest antenna efficiency of 52% at 3.42 GHz, and the efficiency at other resonant frequencies has also increased in comparison to its previous model. Multiple SRR structures can be used to modify the current distribution on the patch and ground planes, resulting in improved bandwidth.

Overall, using SRR structures in more than one way can help patch antennas work in multiband by adding more resonant frequencies, increasing bandwidth, making it easier to design small antennas, and reducing mutual coupling. These benefits can enable the creation of a compact and efficient multiband patch antenna that can operate over a wide frequency range.

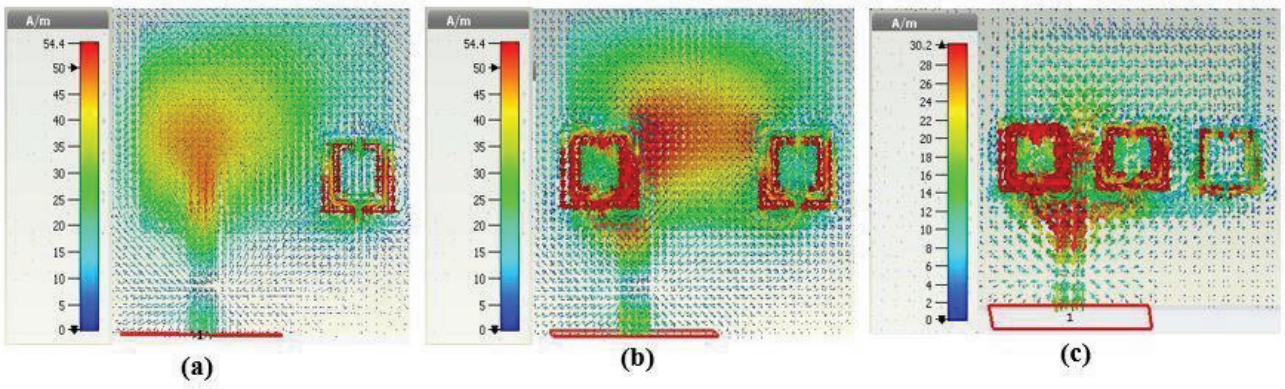


**Fig. 14.** Surface current distribution of proposed MTM loaded multiband antennas (a) Model-1 (with 1 SRR), (b) Model-2 (with 2 SRR), and (c) Model-3 (with 3 SRR)

**Table 10:** Simulation results of the conventional MPA and the proposed MTM loaded multiband antenna.

| Antenna configuration | Frequency (GHz) | Return loss (dB) | Bandwidth (MHz) | Gain (dB) | Efficiency | Application |
|---|---|---|---|---|---|---|
| **Conventional patch antenna (without SRR)** | 2.45 | -18 | 64 | 3.79 | 45% | **2.45GHz:** Bluetooth, WiFi, and data communications **~3 GHz:** Television broadcasting, military and local mobile radio transmissions, traffic control, marine and air navigation systems. **~4 GHz:** C Band (Satellite Downlink), Government Authorities and Military Institutions. **~5 GHz:** wireless communication, baby monitoring system and vegetation characteristics analysis **~ 6 GHz:** Airtime efficiency and Satellite Uplink |
| **Model-1 (with 1 SRR)** | 4.03 | -19 | 95 | 2.88 | 50% | |
| | 5.02 | -23 | 158 | 3.88 | 50% | |
| | 5.93 | -14 | 126 | -2.88 | 35% | |
| **Model- 2 ( with 2 SRR)** | 3.13 | -23 | 75 | 1.98 | 45% | |
| | 5.04 | -32 | 167 | 3.68 | 52% | |
| | 6.03 | -36 | 190 | -4.26 | 37% | |
| **Model-3 (with 3 SRR)** | 3.04 | -22 | 78 | 2.08 | 48% | |
| | 3.42 | -26 | 93 | 2.36 | 52% | |
| | 5.35 | -29 | 167 | 3.5 | 49% | |
| | 6.08 | -21 | 185 | -4.38 | 33% | |

## 4. Conclusion

This paper describes how metamaterials can miniaturize and improve antennas and build quarter-wavelength antennas due to their small size and ability to propagate over an endless range of wavelengths. The proposed designs of metamaterial loaded microstrip patch antennas (MPA) have a 75% smaller antenna size than conventional MPA and a higher gain of 5.28 dB. This antenna can be used for satellite communication, long-range Wi-Fi, and cellular networks to enable long-distance communication with reduced interference and enhanced signal quality. In radar systems, antennas with a high gain can be utilized for detection, tracking, and imaging applications. Furthermore, the proposed multiband antenna exhibits quad band operations for S-band and C-band simultaneously. The parallel-connected resonators in the multiband antenna produce twice as much voltage as a single-layered resonator, and the proposed antenna is capable of harvesting more energy than a conventional antenna, and can be used as a rectenna device in any dense forest. Additionally, the proposed multiband antenna design can be used in various communication

systems that require multiple frequency bands. The findings of this study show the potential of metamaterials in antenna design, and further research can lead to the development of more efficient and compact antennas for various applications. It is worth noting that the proposed designs were only simulated using computer simulation technology, and no experimental results were presented. Therefore, the performance of the proposed antennas in real-world scenarios is unknown and requires further investigation. Additionally, the proposed designs were only tested using FR-4 substrate material, and the performance may vary when using other substrate materials.

**References**


1. R. Vadivelu,, and K. Sankaranarayanan. "Cognitive radio: a new standard in wireless communication technology." *Bonfring International Journal of Networking Technologies and Applications* Vol. 1, no. 1, 2012.
2. C. X. Mao, Y. Zhang, X. Y. Zhang, P. Xiao, Y. Wang & S. Gao. "Filtering antennas: Design methods and recent developments." *IEEE Microwave Magazine*, Vol. 22, no. 11, pp. 52-63, 2021.
3. W. J. Krzysztofik, & T. N. Cao. "Metamaterials in application to improve antenna parameters." *Metamaterials and Metasurfaces*, Vol. 12, no. 2, pp. 63-85, 2018.
4. R. Kumar, M. Kumar, J.S. Chohan, & S. Kumar. "Overview on metamaterial: History, types and applications." *Materials Today: Proceedings*, Vol. 56, pp. 3016-3024, 2022.
5. H.A. Majid, M.K.A. Rahim & T. Masri. "Left handed metamaterial design for microstrip antenna application." In 2008 *IEEE International RF and Microwave Conference*, pp. 218-221, 2008.
6. H.A. Majid, M.K. Abd Rahim & T. Masri. "Microstrip antenna's gain enhancement using left-handed metamaterial structure." *Progress In Electromagnetics Research M*, Vol. 8, pp. 235-247, 2009.
7. E. Dogan, E. Unal, D. Kapusuz, M. Karaaslan, & C. Sabah. "Microstrip patch antenna covered with left handed metamaterial." *The Applied Computational Electromagnetics Society Journal (ACES)*, pp. 999-1004, 2013.
8. R. Kubacki, S. Lamari, M. Czyżewski & D. Laskowski. "A broadband left-handed metamaterial microstrip antenna with double-fractal layers." *International Journal of Antennas and Propagation*, 2017.
9. A.H. Rambe, T. Angriani, F. Fahmi, & S. Alim. "Size reduction of the square microstrip patch antenna with Koch fractal for 1.575 GHz applications." *In Journal of Physics: Conference Series*, vol. 2421, no. 1, p. 012-042, 2023.
10. T. Upadhyaya, R. Pandey, U. Patel, K. Pandya, A. Desai, R. Patel & Y. Kosta. "Left-Handed material inspired multi-layer planar antenna design for satellite communication applications." *Progress In Electromagnetics Research M,* Vol. 108, pp. 201-211, 2022.
11. R. Mishra (2016). "An overview of microstrip antenna." *HCTL Open International Journal of Technology Innovations and Research (IJTIR), Vol.* 21, no. 2, pp. 39-55, 2016.
12. N.J. Shimu, & A. Ahmed. "Design and performance analysis of rectangular microstrip patch antenna at 2.45 GHz." In 2016 *5th International Conference on Informatics, Electronics and Vision (ICIEV)*, pp. 1062-1066, 2016.
13. D.M. Pozar (1992). "Microstrip antennas." *Proceedings of the IEEE*, Vol. 80, no. 1, pp. 79-91, 1992.
14. M. Gil, J. Bonache, J. Garcia-Garcia, J. Martel, & F. Martin. "Composite right/left-handed metamaterial transmission lines based on complementary split-rings resonators and their applications to very wideband and compact filter design." *IEEE transactions on microwave theory and techniques*, Vol. 55, no. 6, pp. 1296-1304, 2007.
15. C.A. Balanis. *Antenna theory: analysis and design*. John wiley & sons, 2016.
16. J.D. Baena, J. Bonache, F. Martin, R.M. Sillero, F. Falcone, T. Lopetegi, ... & M. Sorolla., "Equivalent circuit models for split ring resonators and complementary split ring resonators coupled to planar transmission lines". IEEE Transactions Microwave Theory and Techniques, Vol. 53, no. 4, pp. 1451-1461, 2005.
17. M.F. Wu, F.Y. Meng, Q. Wu, J. Wu & L.W. Li. "A compact equivalent circuit model for the SRR structure in Metamaterials", Microwave Conference Proceedings, APMC, 2005.
18. Q. Wu, M.F. Wu, F.Y. Meng, J. Wu & L.W. Li. "Modeling The Effects of an Individual SRR by Equivalent Circuit Method", IEEE Antennas and Propagation Society International Symposium, Vol. 1B, pp 631-634, 2005.
19. S. Naoui, L. Latrach & A. Gharsallah. "Equivalent circuit model of double split ring resonators." *Int. J. Microw. Opt. Technol*, Vol. 1, no. 1, pp. 1-6, 2016.
20. N. Hamzah & K.A. Othman. "Designing Vivaldi antenna with various sizes using CST software." In Proceedings of the World Congress on Engineering, vol. 2, pp. 6-8. 2011.
21. P.C. Kar & M.A. Islam. "Design and performance analysis of a rectenna system for charging a mobile phone from ambient EM waves." *Heliyon*, Vol. 9, no. 3, 2023.